Article type: Research Article

High-Entropy Intermetallic PtRhBiSnSb Nanoplates for Highly Efficient Alcohol Oxidation Electrocatalysis

Wen Chen[#], Shuiping Luo[#], Mingzi Sun[#], Xiaoyu Wu, Yongsheng Zhou, Yujia Liao, Min Tang, Xiaokun Fan, Bolong Huang and Zewei Quan**

Dr. W. Chen
School of Chemistry and Chemical Engineering, Harbin Institute of Technology, Harbin 15001, China

Dr. W. Chen, Dr. S. Luo, Dr. X. Wu, Y. Zhou, Y. Liao, Dr. M. Tang, Dr. X. Fan, Prof. Z. Quan
Department of Chemistry and Academy for Advanced Interdisciplinary Studies, Southern University of Science and Technology (SUSTech), Shenzhen, Guangdong 518055, China
*E-mail: quanzw@sustech.edu.cn

Dr. M. Sun, Prof. B. Huang
Department of Applied Biology and Chemical Technology, The Hong Kong Polytechnic University, Hung Hom, Kowloon, Hong Kong SAR, China
*E-mail: bhuang@polyu.edu.hk

Keywords: high-entropy intermetallic; electrocatalysis; alcohol oxidation; nanoplate.

Abstract: The control of multimetallic ensembles at the atomic-level is challenging, especially for the high-entropy alloys (HEAs) possessing five or more elements. Herein, we report the one-pot synthesis of hexagonal close packed (*hcp*) PtRhBiSnSb high-entropy intermetallic (HEI) nanoplates with intrinsically isolated Pt, Rh, Bi, Sn, and Sb atoms, to boost the electrochemical oxidation of liquid fuels. Taking advantage of these combined five metals, the well-defined PtRhBiSnSb HEI nanoplates exhibit a remarkable mass activity of 19.529, 15.558, and 7.535 A mg^{-1}_{Pt+Rh} towards the electrooxidation of methanol, ethanol, and glycerol in alkaline electrolytes, respectively, representing a state-of-the-art multifunctional electrocatalyst for alcohol oxidation reactions. In particular, the PtRhBiSnSb HEI achieves the record-high methanol oxidation reaction (MOR) activity in the alkaline environment. Theoretical calculations have demonstrated the introduction of the fifth metal Rh enhances the electron transfer efficiency in PtRhBiSnSb HEI nanoplates, which contributes to the improved oxidation capability. Meanwhile, the robust electronic structures of active sites are achieved due to the

synergistic protections from Bi, Sn, and Sb sites. This work has offered significant research advances in developing well-defined HEA with delicate control over compositions and properties.

1. Introduction

Direct alcohol fuel cells (DAFCs) have attracted extensive attention in sustainable power supplies, as they employ liquid alcohol fuels that are safe, efficient, and easy to produce, store, and transport under ambient conditions compared to hydrogen.[1-5] However, the alcohol oxidation reactions (AORs) such as methanol oxidation reaction (MOR), ethanol oxidation reaction (EOR), and glycerol oxidation reaction (GOR) are kinetically sluggish processes, and various reaction intermediates involved in the AORs call for active site ensembles with multifunctions.[6-10] The engineering of multimetallic Pt-based electrocatalysts (typically $\leqslant$ three elements) effectively boosts the AORs electrocatalysis due to the strain, electronic, ensemble, and bifunctional effects.[11-16]

In particular, HEAs have emerged as a unique class of multimetallic alloys, which generally consist of five or more metals and show great room for improvement in their geometric and electronic structures and their catalytic properties.[17-26] Compared with alloy nanocrystals with typically disordered phases, intermetallic nanocrystals exhibit long-range ordered and well-defined compositions, which can be delicately manipulated to clarify the structure-property relationship.[27-33] Combining the advantages of HEAs and intermetallic compounds, HEIs are promising candidates as multifunctional electrocatalysts, yet they have been rarely explored due to the difficulties in syntheses, characterizations, calculations, etc.[34-39]

Herein, inspired by the same *hcp* crystalline structures of PtBi, RhBi, PtSn, and PtSb intermetallics, we report the first synthesis of PtRhBiSnSb HEI nanoplates via a facile wet-chemistry method (**Figure S1, the Supporting Information**). The atomic-resolution image and simulation results reveal the substitution of Rh atoms on Pt columns and the substitution of Sn/Sb atoms on Bi columns in this *hcp* PtBi-type (PtRh)(BiSnSb) HEI. The synergistic effects

of Pt/Rh/Bi/Sn/Sb atoms endow PtRhBiSnSb HEI nanoplates with ultra-high mass activities of 19.529, 15.558, and 7.535 A mg^{-1}_{Pt+Rh} at the peak potentials towards MOR, EOR, and GOR, respectively. In addition, the PtRhBiSnSb HEI nanoplates retain 70.2% of the initial MOR activity after sweeping for 5000 cycles, exhibit stable current densities over the operation for 20000 s, and avoid CO poisoning. Density functional theory (DFT) calculations reveal that the superior alcohol oxidation performances of PtRhBiSnSb HEI nanoplates mainly originate from the introduction of Rh metal, to facilitate the efficient electron transfer and high electroactivity. The synergistic contributions of Bi, Sn, and Sb reach the robust valence states of Pt and Rh in PtRhBiSnSb HEI nanoplates, which guarantee efficient and durable electrocatalysis.

2. Results and Discussion

The PtRhBiSnSb HEI nanoplates were fabricated by a facile one-pot thermal decomposition of platinum acetylacetonate [$Pt(acac)_2$], rhodium acetylacetonate [$Rh(acac)_3$], bismuth acetate [$Bi(act)_3$], stannous chloride ($SnCl_2$), and antimonous chloride ($SbCl_3$) in the mixture of oleylamine (OAM), octadecene (ODE), ascorbic acid (AA), and cetyltrimethylammonium bromide (CTAB) at 220 ℃. The transmission electron microscopy (TEM, **Figure 1a**) and high-angle annular dark-field scanning transmission electron microscopy (HAADF-STEM, **Figure S2**) images show that the products are well-dispersed hexagonal nanoplates, of which the average edge length is about 6.2 nm. The X-ray diffraction (XRD) patterns in **Figures 1b and S3** reveal that the PtRhBiSnSb HEI nanoplates exhibit the typical *hcp* crystalline structure, which is similar to those of binary *hcp* PtBi/RhBi/PtSn/PtSb/ intermetallics. The atomic ratio of Pt/Rh/Bi/Sn/Sb is determined to be 38.0/9.8/32.2/9.8/10.2 by inductively coupled plasma mass spectrometry (ICP-MS), which is in good agreement with the energy-dispersive X-ray spectroscopy (EDX) results in **Figure S4** (Pt/Rh/Bi/Sn/Sb = 37.9/9.7/31.7/8.8/11.9). In addition, the sum of the atomic percentages of Pt and Rh (Pt + Rh = 47.8%) is basically the same as that of Bi, Sn, and Sb (Bi + Sn + Sb = 52.2%), indicating the formation of well-defined *hcp* (PtRh)(BiSnSb) HEI nanoplates.[36, 40]

The atomic structure of the PtRhBiSnSb HEI nanoplates is uncovered by the aberration-corrected HAADF-STEM characterizations. The ordered atomic arrangements in PtRhBiSnSb HEI nanoplates are revealed by the well-defined stacking sequences of atomic columns throughout the nanoplates projected along the top-view [001] and side-view [110]/[210] zone axes, respectively (**Figures 1c-f, S5, and S6**), which are consistent with the atomic arrangements in *hcp* PtBi intermetallic.[7, 11] Especially, the regular arrangements of two dark dots and one bright dot on the edge of nanoplates are clearly observed in the [001] orientation (**Figure 1d**), which can be easily indexed to the Bi-type columns and Pt-type columns based on the *hcp* PtBi intermetallic structure, respectively. As shown in **Figure 1c**, the lattice spacing of the (100) planes on the edge of nanoplates is measured to be ~0.361 nm, which is located between that of (100) planes in PtBi (0.374 nm), PtSn (0.355 nm) and PtSb (0.358 nm) intermetallics. In addition, the consistent lattice spacing of 0.204 nm indicates the identical *hcp* crystal structure across the nanoplate, while the brightness distribution throughout the nanoplate varies, which should originate from the distinct atomic distributions of Pt/Rh/Bi/Sn/Sb in different sections. Based on the EDX mapping results in **Figure 1h** and **Figure S7,** the atomic percentages of Rh and Bi are relatively higher in the central parts of the nanoplate, and the atomic percentages of Pt, Sn, and Sb are relatively higher near the nanoplate edges. **Figure 1g** shows the possible structural model of the as-synthesized PtRhBiSnSb HEI nanoplates, illustrating a novel class of fully ordered *hcp* quinary nanoplates with intrinsically isolated Pt, Rh, Bi, Sn, and Sb atoms.

Different from the PtBi-type atomic arrangements, the central parts of the PtRhBiSnSb HEI nanoplates viewed along the [001] direction exhibit a new periodic stacking pattern, which can be used to resolve its atomic arrangements (**Figure 2a**). In this HAADF-STEM image, bright and dark spots arranged periodically in a rhombus are observed. The intensity profile analyses across the as-indicated lines (**Figure 2b**) demonstrate that there are three types of atomic configurations, as shown in the plot 1, 2, and 3, respectively. A two-dimensional (2D) Gaussian

fitting of the positions and intensities of the bright spots in the HAADF image (**Figures 2c-d and S8)** clearly reveals the intensity variation.[41-45] The intensities of the six intermediate Pt-site atomic columns (grey circle) around the central Pt-site column are significantly weaker than those of the six outermost Pt-site atomic columns (red circle), which should be attributed to the substitution of Pt with Rh. By replacing the Pt atoms at the intermediate Pt-site atomic columns (grey circle) with 80%Rh + 20%Pt atoms, the theoretical atomic model is constructed (**Figure 2f)**, from which the corresponding simulated image is obtained (**Figures 2e and S8**). The intensities of these atoms and three atomic configurations (plot 1, 2, and 3) in **Figures 2a-c** are basically consistent with those obtained from the corresponding simulated image. As for the near edge parts of the PtRhBiSnSb HEI nanoplates viewed along [001] direction, the periodic stacking pattern is consistent with the model, in which the Pt atoms are replaced by 20%Rh + 80%Pt atoms at the intermediate Pt-site atomic columns (grey circle, **Figure S9**). At this stage, the atomic structure of (PtRh)(BiSnSb) HEI nanoplates is successfully identified, as shown in **Figure 2h**. In addition, as indicated by the XPS spectra in **Figures 2g** and **S10**, Pt and Rh atoms are mainly in the zero-valence state, while Bi, Sn, and Sb atoms are mainly in their oxidation states, due to the exposure of the easily oxidizable Bi, Sn and Sb atoms on the surface.[46-50] As shown in the Pt 4f XPS spectra of different Pt-based nanoparticles **(Figure S11)**, PtRhBiSnSb HEI nanoplates exhibit the lowest Pt 4f binding energy that could contribute to the weaker bonding strength between the catalyst surface and the adsorbed intermediate species, thus ensuring a higher electrocatalytic activity.[51-52]

The uniform (PtRh)(BiSnSb) HEI nanoplates are obtained via a facile one-pot method, in which the Pt+Rh/Sn+Bi+Sb ratio should be kept at about 1:1. The time-dependent evolutions of crystalline structure, composition, and morphology during the synthesis of PtRhBiSnSb HEI nanoplates are explored (see **Figures S12-14** for details), revealing a typical "complexing-reducing-ordering" growth process in this one-pot method. Especially, Bi-complex is formed at the beginning as the template for the growth of nanoplates, Rh and Sb atoms are merged into

those nanoplates at the later stage compared with Pt and Sn atoms, and the diffusion and ordering of Pt/Rh/Bi/Sn/Sb atoms produce well-defined (PtRh)(BiSnSb) HEI nanoplates with good uniformity.[11] As an important control sample (**Figure S15**), the PtBiSnSb intermetallic nanoplates with pure *hcp* phase are fabricated as well (Pt/Bi/Sn/Sb = 46.1/30.0/12.1/11.8, obtained by ICP-MS). The EDX mapping images of PtBiSnSb intermetallic nanoplates reveal the uniform distribution of Pt, Bi, Sn, and Sb elements over the hexagonal nanoplate (**Figure S15e**).

The PtRhBiSnSb, PtBiSnSb, and PtBi nanoplates[11] are dispersed on the commercial carbons (Pt loadings are ~10 wt%) and washed by a hexane/ethanol/1-butylamine mixture, and then their electrocatalytic properties are systemically evaluated in alkaline electrolytes. **Figure 3a** shows the cyclic voltammograms (CVs) of these electrocatalysts recorded in the Ar-saturated 1.0 M KOH solution. Compared with the commercial Pt/C electrocatalyst, the hydrogen adsorption/desorption peaks (0.05 V to 0.5 V vs. RHE) of the PtRhBiSnSb, PtBiSnSb, and PtBi intermetallic catalysts are obviously suppressed, due to the isolated Pt sites on the surface of these *hcp* PtBi-type intermetallics. **Figures 3b-d** show the positive-going MOR, EOR, and GOR polarization curves recorded in the Ar-saturated 1.0 M KOH + 1.0 M CH_3OH, 1.0 M KOH + 1.0 M C_2H_5OH, and 1.0 M KOH + 0.1 M $C_3H_5(OH)_3$ electrolytes at 30 °C, respectively. The PtBi nanoplates show slightly higher MOR, EOR, and GOR activities than the Pt/C electrocatalyst, and the PtBiSnSb nanoplates exhibit much higher activities than the PtBi nanoplates. With the mixture of isolated Pt/Rh/Bi/Sn/Sb atoms, the as-obtained PtRhBiSnSb HEI nanoplates achieve the highest MOR, EOR, and GOR peak mass activities of 19.529 A mg^{-1}_{Pt+Rh}, 15.558 A mg^{-1}_{Pt+Rh}, and 7.535 A mg^{-1}_{Pt+Rh} (**Figure S16**), obviously higher than those of PtBiSnSb nanoplates and 8.6/10.4/7.6 times higher than those of Pt/C electrocatalyst, respectively. These results suggest a synergistic effect of these five metals in boosting AORs.[49, 53-54] To the best of our knowledge, the PtRhBiSnSb HEI nanoplates emerge as a state-of-the-

art electrocatalyst for AORs, and notably reach the record-high MOR activities in alkaline electrolytes (**Tables S1-3**).[7, 46, 55-60]

The electrochemical durabilities of the highly active PtRhBiSnSb HEI nanoplates and PtBiSnSb nanoplates are evaluated by sweeping 5000 CV cycles in the 1.0 M KOH + 1.0 M CH_3OH solution. As shown in **Figure 3e**, after 5000 cycles, the current densities (calculated at the peak potentials of ≈0.85 V vs RHE) of PtRhBiSnSb and PtBiSnSb retain 70.2% and 62.7% of their initial values, respectively, while the Pt/C electrocatalyst retains 23.1%. In addition, the chromoamperometric (CA) measurements of PtRhBiSnSb HEI nanoplates for MOR, EOR, and GOR are evaluated at 0.7 V, 0.65 V, and 0.65 V versus RHE for 20000 s, respectively, and those potentials are chosen based on their different polarization curves (**Figures 3f** and **S17**). As revealed by the much higher current densities compared with the Pt/C electrocatalyst in those CA curves, the PtRhBiSnSb HEI nanoplates exhibit excellent long-term durability toward AORs. Moreover, the multimetallic compositions of PtRhBiSnSb HEI nanoplates (**Figure S18**) and PtBiSnSb nanoplates (**Figure S19**) are basically maintained, and the partial leaching of Bi atoms could lead to the decay of their activities. As shown in the CO-stripping experiments (**Figures 3g** and **S20**), the oxidation peaks at around 0.7 V vs. RHE of the absorbed CO are significantly suppressed on the PtRhBiSnSb HEI, PtBiSnSb, and PtBi nanoplates compared to the Pt/C, indicating their superior tolerances to CO poisoning. The results are attributed to the exposure of Bi/Sn/Sb species and the isolated Pt sites on the surface of these *hcp* PtBi-type intermetallic nanoplates.

Considering the superior MOR electrocatalytic performances of PtRhBiSnSb HEI nanoplates, **Figures 3h** and **S21** show the *in situ* fourier transform infrared (FTIR) and attenuated total reflection-surface enhanced infrared absorption (ATR-SEIRA) spectra of PtRhBiSnSb HEI nanoplates and Pt/C for MOR in alkaline electrolyte. During the MOR process, methanol is first oxidized to $HCOO^-$ (asymmetric stretching vibration band of $HCOO^-$ at ~ 1585 cm^{-1} and symmetric vibration twin bands of $HCOO^-$), and then $HCOO^-$ is further oxidized to CO_2

(vibration band of CO_2 at ~ 2345 cm^{-1}), and finally, the adsorbed CO_2 is desorbed and reacted with OH to form CO_3^{2-}/HCO_3^- (wide vibration band of CO_3^{2-}/HCO_3^- at ~ 1376 cm^{-1}). The onset potentials corresponding to these characteristic peaks of PtRhBiSnSb HEI nanoplates are 100 mV lower than those of Pt/C, further supporting the superior MOR electrocatalytic performances on PtRhBiSnSb HEI nanoplates. Furthermore, the ATR-SEIRA spectra in **Figure S21b-c** show there is no CO_L signal (linearly bonded of CO_{ad} (CO_L) species at ~ 2050 cm^{-1}) over the entire potential range on PtRhBiSnSb HEI nanoplates, revealing that methanol is oxidized through a CO-free pathway. Thus, the classical CO-poisoning issue on the Pt-based catalysts is vanished on this PtRhBiSnSb HEI electrocatalyst, due to its superior tolerance toward CO-poisoning and optimized MOR pathway to avoid CO-poisoning.[46, 61-65]

DFT calculations have been introduced to further explore the alcohol oxidation performances of the PtRhBiSnSb HEI nanoplates. Compared with the PtBiSnSb nanoplates, the introduction of Rh on the Pt sites further improves the electroactivity (**Figures 4a-b, S22**). Notably, the contributions of surface bonding near the Fermi level (E_F) to PtRhBiSnSb HEInanoplates become larger, especially on the Rh sites, indicating the introduction of Rh further enhances the electroactivity. The overall structure of the PtRhBiSnSb HEI nanoplates and PtBiSnSb nanoplates are both stable without evident lattice distortions, indicating the promising durability of the electrocatalyst. The projected partial density of states (PDOSs) are demonstrated to unravel the contributions of electronic structures (**Figure 4c**). Notably, Rh-4d orbitals show an evident peak near the E_F while the Pt-5d orbitals locate at a slightly lower position at E_V-2.28 eV (E_V = 0 eV). Meanwhile, the p orbitals from Sb, Bi, and Sn exhibit similar broad orbitals that cross the E_F, indicating efficient electron transfer. Moreover, the efficient p-d orbital coupling enables the stabilization of valence states on Pt and Rh sites by the Bi, Sn, and Sb sites. The electronic structure comparison with the PtBiSnSb also shows that the overall d-band center has evidently increased after the introduction of Rh, supporting the improved electron transfer efficiency of the electrocatalyst (**Figure 4d**). Meanwhile, the surface Pt sites have

shown a slightly decreased d-band center, which suppresses the overbinding of the intermediates to guarantee efficient electrocatalysis. To further identify the electronic modulations, the site-dependent PDOSs of each element are supplied in PtRhBiSnSb HEI nanoplates. For Pt sites, the Pt-5d orbitals show a gradual upshifting from the bulk to the surface (**Figure 4e**). Notably, the surrounding Sn and Sb sites further improve the electroactivity of Pt due to the closer position to the E_F. In the meantime, the Rh-4d orbitals remain a highly robust electronic structure from the bulk to the surface, exhibiting the strong electron depletion capability for the oxidation process (**Figure 4f**). The doping of Rh on Pt sites does not affect the electroactivity of neighboring Pt sites and supplies additional active sites for the oxidation reactions, and the site-dependent PDOSs of both Pt and Rh support the improved electroactivity and stable valence states due to the introduction of Sn and Sb. Bi sites display the broad 6p orbitals in different sites in the electrocatalysts (**Figure 4g**). However, the electron density near the E_F increases from the bulk to the surface, especially near the introduced Rh atoms, leading to efficient electron transfer via the p-d coupling. For both Sn-5p and Sb-5p, highly robust electronic structures have been shown, where the valence states are not strongly affected by the positions (**Figures 4h-i**). From the PDOSs, Bi, Sn, and Sb sites are prone to be oxidized due to the low barriers for electron depletion, which mainly play as the buffer sites to protect the metallic Pt and Rh sites with high electroactivity within PtRhBiSnSb HEI nanoplates from oxidization during the MOR.

Then, the performances of PtRhBiSnSb HEI nanoplates and PtBiSnSb nanoplates are compared from the energetic perspective. Notably, the adsorption of CH_3OH and CO_2 are strengthened in PtRhBiSnSb HEI nanoplates, leading the improved electroactivity towards the oxidation of CH_3OH (**Figure 4j**). Meanwhile, the PtRhBiSnSb HEI nanoplates show an unpreferred adsorption CO, which supports the stronger resistance towards the CO poisoning during the MOR. For the CO_2 pathways, it is noted that the PtRhBiSnSb HEI nanoplates deliver a stronger reaction trend with one minor energy barrier of 0.41 eV at CHOH* to CHO*

conversion (**Figure 4k**), in contrast, the PtBiSnSb nanoplates show several larger energy barriers during the MOR. Moreover, PtRhBiSnSb HEI nanoplates display more negative reaction energy than PtBiSnSb nanoplates, which further reveals their superior MOR performance. Meanwhile, for the CO pathway, the energy barrier of 0.77 eV on PtRhBiSnSb HEI nanoplates is much larger than that of the CO_2 pathway, indicating a stronger selectivity toward the CO_2 (**Figure 4l**). On the other side, PtBiSnSb nanoplates show a stronger preference towards the CO pathway, leading to the relatively lower performance of alcohol oxidation.

3. Conclusion

In summary, we successfully construct the well-defined PtRhBiSnSb HEI nanoplates and confirm the formation of the *hcp* (PtRh)(BiSnSb) crystalline structure by substituting Sn/Sb atoms at Bi sites and Rh atoms at Pt sites. Enabled by the synergistic effect of these five metals, the PtRhBiSnSb HEI nanoplates exhibit super-high mass activities and excellent durabilities towards MOR (record-high value), EOR, and GOR, representing a state-of-the-art multifunctional electrocatalyst for alcohol oxidations. DFT calculations have indicated the optimization of electronic structures in PtRhBiSnSb HEI nanoplates by the introduction of Rh, which not only improves the electron transfer but also the electroactivity with an optimal d-band center. The optimized electronic structure leads to stronger selectivity and durability for the CO_2 reaction pathways of alcohol oxidations. This work offers an effective and practical strategy to achieve and resolve the atomically long-range ordered HEI, thus developing multifunctional catalysts with unprecedented properties.

4. Experimental Section

Experimental details are provided in the Supporting Information.

Supporting Information

Supporting Information is available from the Wiley Online Library or from the author.

Acknowledgements

W. C., S. L., and M. S. contributed equally to this work. This work was supported by the National Natural Science Foundation of China (NSFC) (Grants 52072166, 52101259 and 21771156), the Guangdong Science and Technology Department (Grants 2016ZT06C279 and 2022A1515010918), the Shenzhen Science and Technology Innovation Committee (Grants JCYJ20210324105008022, KQTD20160530191343 56 and RCJC20210609104441 06), the NSFC/RGC Joint Research Scheme Project (N_PolyU502/21), and the funding for Projects of Strategic Importance of The Hong Kong Polytechnic University (Project Code: 1-ZE2V). The authors acknowledge the assistance of Dr. Wu Wang for his help in analyzing the HRTEM results of SUSTech Core Research Facilities.

Received: ((will be filled in by the editorial staff))
Revised: ((will be filled in by the editorial staff))
Published online: ((will be filled in by the editorial staff))

References

[1] Z. W. Seh, J. Kibsgaard, C. F. Dickens, I. Chorkendorff, J. K. Nørskov, T. F. Jaramillo, *Science* **2017**, *355*, eaad4998.

[2] M. Li, Z. Zhao, W. Zhang, M. Luo, L. Tao, Y. Sun, Z. Xia, Y. Chao, K. Yin, Q. Zhang, L. Gu, W. Yang, Y. Yu, G. Lu, S. Guo, *Adv. Mater.* **2021**, *33*, 2103762.

[3] R. Rizo, B. Roldan Cuenya, *ACS Energy Lett.* **2019**, *4*, 1484.

[4] J. T. L. Gamler, H. M. Ashberry, S. E. Skrabalak, K. M. Koczkur, *Adv. Mater.* **2018**, *30*, 1801563.

[5] J. Zhang, M. Yuan, T. Zhao, W. Wang, H. Huang, K. Cui, Z. Liu, S. Li, Z. Li, G. Zhang, *J. Mater. Chem. A* **2021**. *9*, 20676.

[6] W. Zhang, Y. Yang, B. Huang, F. Lv, K. Wang, N. Li, M. Luo, Y. Chao, Y. Li, Y. Sun, Z. Xu, Y. Qin, W. Yang, J. Zhou, Y. Du, D. Su, S. Guo, *Adv. Mater.* **2019**, *31*, 1805833.

[7] S. Luo, L. Zhang, Y. Liao, L. Li, Q. Yang, X. Wu, X. Wu, D. He, C. He, W. Chen, Q. Wu, M. Li, E. J. M. Hensen, Z. Quan, *Adv. Mater.* **2021**, *33*, 2008508.

[8] X. Wang, S. Xi, W. S. V. Lee, P. Huang, P. Cui, L. Zhao, W. Hao, X. Zhao, Z. Wang, H. Wu, H. Wang, C. Diao, A. Borgna, Y. Du, Z. G. Yu, S. Pennycook, J. Xue, *Nat. Commun.* **2020**, *11*, 4647.

[9] Z. Chen, C. Liu, X. Zhao, H. Yan, J. Li, P. Lyu, Y. Du, S. Xi, K. Chi, X. Chi, H. Xu, X. Li, W. Fu, K. Leng, S. J. Pennycook, S. Wang, K. P. Loh, *Adv. Mater.* **2019**, *31*, 1804763.

[10] J. Han, Y. Kim, D. H. K. Jackson, H. Chang, H. W. Kim, J. Lee, J. R. Kim, Y. Noh, W. B. Kim, K. Y. Lee, H. J. Kim, *Appl. Catal. B - Environ.* **2020**, *273,* 119037.

[11] S. Luo, W. Chen, Y. Cheng, X. Song, Q. Wu, L. Li, X. Wu, T. Wu, M. Li, Q. Yang, K. Deng, Z. Quan, *Adv. Mater.* **2019**, *31*, 1903683.

[12] H. l. Liu, F. Nosheen, X. Wang, *Chem. Soc. Rev.* **2015**, *44*, 3056.

[13] J. Zhu, Y. Yang, L. Chen, W. Xiao, H. Liu, H. D. Abruña, D. Wang, *Chem. Mater.* **2018**, *30*, 5987.

[14] S. Luo, P. K. Shen, *ACS Nano* **2016**, *11*, 11946.

[15] L. Bu, N. Zhang, S. Guo, X. Zhang, J. Li, J. Yao, T. Wu, G. Lu, J. Y. Ma, D. Su, X. Huang, *Science* **2016**, *354*, 1410.

[16] Z. Zhang, Z. Luo, B. Chen, C. Wei, J. Zhao, J. Chen, X. Zhang, Z. Lai, Z. Fan, C. Tan, M. Zhao, Q. Lu, B. Li, Y. Zong, C. Yan, G. Wang, Z. J. Xu, H. Zhang, *Adv. Mater.* **2016**, *28*, 8712.

[17] Y. Xin, S. Li, Y. Qian, W. Zhu, H. Yuan, P. Jiang, R. Guo, L. Wang, *ACS Catal.* **2020**, *10*, 11280.

[18] H. Li, J. Lai, Z. Li, L. Wang, *Adv. Funct. Mater.* **2021**, *31,* 2106715.

[19] Y. Zhang, D. Wang, S. Wang, *Small* **2022**, *18*, 2104339.

[20] K. V. Yusenko, S. Riva, P. A. Carvalho, M. V. Yusenko, S. Arnaboldi, A. S. Sukhikh, M. Hanfland, S. A. Gromilov, *Scr. Mater.* **2017**, *138*, 22.

[21] Y. Yao, Q. Dong, A. Brozena, J. Luo, J. Miao, M. Chi, C. Wang, I. G. Kevrekidis, Z. J. Ren, J. Greeley, G. Wang, A. Anapolsky, L. Hu, *Science* **2022**, *376*, eabn3103.

[22] Y. Liao, Y. Li, R. Zhao, J. Zhang, L. Zhao, L. Ji, Z. Zhang, X. Liu, G. Qin, X. Zhang, *Natl. Sci. Rev.* **2022**, nwac041.

[23] G. Feng, F. Ning, J. Song, H. Shang, K. Zhang, Z. Ding, P. Gao, W. Chu, D. Xia, *J. Am. Chem. Soc.* **2021**, *143*, 17117.

[24] D. Wu, K. Kusada, T. Yamamoto, T. Toriyama, S. Matsumura, S. Kawaguchi, Y. Kubota, H. Kitagawa, *J. Am. Chem. Soc.* **2020**, *142*, 13833.

[25] Y. Yao, Z. Huang, L. A. Hughes, J. Gao, T. Li, D. Morris, S. E. Zeltmann, B. H. Savitzky, C. Ophus, Y. Z. Finfrock, Q. Dong, M. Jiao, Y. Mao, M. Chi, P. Zhang, J. Li, A. M. Minor, R. Shahbazian-Yassar, L. Hu, *Matter* **2021**, *4*, 2340.

[26] C. Zhan, Y. Xu, L. Bu, H. Zhu, Y. Feng, T. Yang, Y. Zhang, Z. Yang, B. Huang, Q. Shao, X. Huang, *Nat. Commun.* **2021**, *12*, 6261.

[27] C. L. Yang, L. N. Wang, P. Yin, J. Liu, M. X. Chen, Q. Q. Yan, Z. S. Wang, S. L. Xu, S. Q. Chu, C. Cui, H. Ju, J. Zhu, Y. Lin, J. Shui, H. W. Liang, *Science* **2021**, *374*, 459.

[28] Y. Yao, Z. Huang, P. Xie, D. Lacey Steven, J. Jacob Rohit, H. Xie, F. Chen, A. Nie, T. Pu, M. Rehwoldt, D. Yu, R. Zachariah Michael, C. Wang, R. Shahbazian-Yassar, J. Li, L. Hu, *Science* **2018**, *359*, 1489.

[29] S. Y. Ma, H. H. Li, B. C. Hu, X. Cheng, Q. Q. Fu, S. H. Yu, *J. Am. Chem. Soc.* **2017**, *139*, 5890.

[30] X. Ji, K. T. Lee, R. Holden, L. Zhang, J. Zhang, G. A. Botton, M. Couillard, L. F. Nazar, *Nat. Chem.* **2010**, *2*, 286.

[31] D. Wang, H. L. Xin, R. Hovden, H. Wang, Y. Yu, D. A. Muller, F. J. DiSalvo, H. D. Abruña, *Nat. Mater.* **2013**, *12*, 81.

[32] Y. Yan, J. S. Du, K. D. Gilroy, D. Yang, Y. Xia, H. Zhang, *Adv. Mater.* **2017**, *29*, 1605997.

[33] S. Zhao, Z. Li, C. Zhu, W. Yang, Z. Zhang, E. J. Armstrong David, S. Grant Patrick, O. Ritchie Robert, A. Meyers Marc, *Sci. Adv.* **2017**, *7*, eabb3108.

[34] A. Dasgupta, H. He, R. Gong, S. L. Shang, E. K. Zimmerer, R. J. Meyer, Z. K. Liu, M. J. Janik, R. M. Rioux, *Nat. Chem.* **2022**, *14*, 523.

[35] D. Wang, Z. Chen, Y. Wu, Y. C. Huang, L. Tao, J. Chen, C. L. Dong, C. V. Singh, S. Wang, *SmartMat.* **2022**, DOI: 10.1002/smm2.1117.

[36] J. Ma, F. Xing, Y. Nakaya, K. I. Shimizu, S. Furukawa, *Angew. Chem. Int. Ed.* **2022**, DOI: 10.1002/anie.202200889.

[37] G. Zhu, Y. Jiang, H. Yang, H. Wang, Y. Fang, L. Wang, M. Xie, P. Qiu, W. Luo, *Adv. Mater.* **2022**, *34*, 2110128.

[38] Y. Lu, K. Huang, X. Cao, L. Zhang, T. Wang, D. Peng, B. Zhang, Z. Liu, J. Wu, Y. Zhang, C. Chen, Y. Huang, *Adv. Funct. Mater.* **2022**, *32*, 2110645.

[39] Z. Jia, T. Yang, L. Sun, Y. Zhao, W. Li, J. Luan, F. Lyu, L. C. Zhang, J. J. Kruzic, J. J. Kai, J. C. Huang, J. Lu, C. T. Liu, *Adv. Mater*. **2020**, *32*, 2000385.

[40] H. Rong, J. Mao, P. Xin, D. He, Y. Chen, D. Wang, Z. Niu, Y. Wu, Y. Li, *Adv. Mater.* **2016**, *28*, 2540.

[41] G. Liu, A. W. Robertson, M. M. Li, W. C. H. Kuo, M. T. Darby, M. H. Muhieddine, Y. C. Lin, K. Suenaga, M. Stamatakis, J. H. Warner, S. C. E. Tsang, *Nat. Chem.* **2017**, *9*, 810.

[42] K. Xu, L. Zhang, A. Godfrey, D. Song, W. Si, Y. Zhao, Y. Liu, Y. Rao, H. Zhang, H. A. Zhou, W. Jiang, W. Wang, Z. Cheng, J. Zhu, *Proc. Natl. Acad. Sci. U. S. A.* **2021**, *118*, e2101106118.

[43] J. Peng, Y. Liu, H. Lv, Y. Li, Y. Lin, Y. Su, J. Wu, H. Liu, Y. Guo, Z. Zhuo, X. Wu, C. Wu, Y. Xie, *Nat. Chem.* **2021**, *13*, 1235.

[44] Z. Qi, C. Xiao, C. Liu, T. W. Goh, L. Zhou, R. Maligal-Ganesh, Y. Pei, X. Li, L. A. Curtiss, W. Huang, *J. Am. Chem. Soc.* **2017**, *139*, 4762.

[45] F. Xing, Y. Nakaya, S. Yasumura, K. i. Shimizu, S. Furukawa, *Nat. Catal.* **2022**, *5*, 55.

[46] W. Chen, S. Luo, M. Sun, M. Tang, X. Fan, Y. Cheng, X. Wu, Y. Liao, B. Huang, Z. Quan, *Small* **2022**, *18*, 2107803.

[47] R. Nie, D. Liang, L. Shen, J. Gao, P. Chen, Z. Hou, *Appl. Catal. B - Environ.* **2012**, *127*, 212.

[48] S. Lee, H. J. Kim, E. J. Lim, Y. Kim, Y. Noh, G. W. Huber, W. B. Kim, *Green Chem.* **2016**, *18*, 2877.

[49] A. Kowal, M. Li, M. Shao, K. Sasaki, M. B. Vukmirovic, J. Zhang, N. S. Marinkovic, P. Liu, A. I. Frenkel, R. R. Adzic, *Nat. Mater.* **2009**, *8*, 325.

[50] K. Jiang, L. Bu, P. Wang, S. Guo, X. Huang, *ACS Appl. Mater. Interfaces* **2015**, *7*, 15061.

[51] B. Hammer, J. K. Nørskov, *Surf. Sci.* **1995**, *343*, 211.

[52] J. K. Nørskov, F. Abild-Pedersen, F. Studt, T. Bligaard, *Proc. Natl. Acad. Sci. U. S. A.* **2011**, *108*, 937.

[53] K. Wang, H. Du, R. Sriphathoorat, P. K. Shen, *Adv. Mater.* **2018**, *30*, 1804074.

[54] N. Erini, V. Beermann, M. Gocyla, M. Gliech, M. Heggen, R. E. Dunin-Borkowski, P. Strasser, *Angew. Chem. Int. Ed.* **2017**, *56*, 6533.

[55] S. Zhang, Z. Zeng, Q. Li, B. Huang, X. Zhang, Y. Du, C. H. Yan, *Energ. Environ. Sci.* **2021**, *14*, 5911.

[56] H. Li, Y. Han, H. Zhao, W. Qi, D. Zhang, Y. Yu, W. Cai, S. Li, J. Lai, B. Huang, L. Wang, *Nat. Commun.* **2020**, *11*, 5437.

[57] J. Chang, G. Wang, M. Wang, Q. Wang, B. Li, H. Zhou, Y. Zhu, W. Zhang, M. Omer, N. Orlovskaya, Q. Ma, M. Gu, Z. Feng, G. Wang, Y. Yang, *Nat. Energy* **2021**, *6*, 1144.

[58] Y. Qiu, J. Zhang, J. Jin, J. Sun, H. Tang, Q. Chen, Z. Zhang, W. Sun, G. Meng, Q. Xu, Y. Zhu, A. Han, L. Gu, D. Wang, Y. Li, *Nat. Commun.* **2021**, *12*, 5273.

[59] H. Pu, K. Dong, T. Zhang, H. Dai, Y. Wang, Y. Deng, *J. Mater. Chem. A* **2022**, *10*, 10614.

[60] F. Yang, J. Ye, Q. Yuan, X. Yang, Z. Xie, F. Zhao, Z. Zhou, L. Gu, X. Wang, *Adv. Funct. Mater.* **2020**, *30*, 1908235.

[61] F. Zhao, J. Ye, Q. Yuan, X. Yang, Z. Zhou, *J. Mater. Chem. A* **2020**, *8*, 11564.

[62] Z. Liang, L. Song, S. Deng, Y. Zhu, E. Stavitski, R. R. Adzic, J. Chen, J. X. Wang, *J. Am. Chem. Soc.* **2019**, *141*, 9629.

[63] J. X. Tang, Q. S. Chen, L. X. You, H. G. Liao, S. G. Sun, S. G. Zhou, Z. N. Xu, Y. M. Chen, G. C. Guo, *J. Mater. Chem. A* **2018**, *6*, 2327.

[64] J. Zhang, X. Qu, Y. Han, L. Shen, S. Yin, G. Li, Y. Jiang, S. Sun, *Appl. Catal. B - Environ.* **2020**, *263*, 118345.

[65] W. Wang, X. Chen, X. Zhang, J. Ye, F. Xue, C. Zhen, X. Liao, H. Li, P. Li, M. Liu, Q. Kuang, Z. Xie, S. Xie, *Nano Energy* **2020**, *71*, 104623.

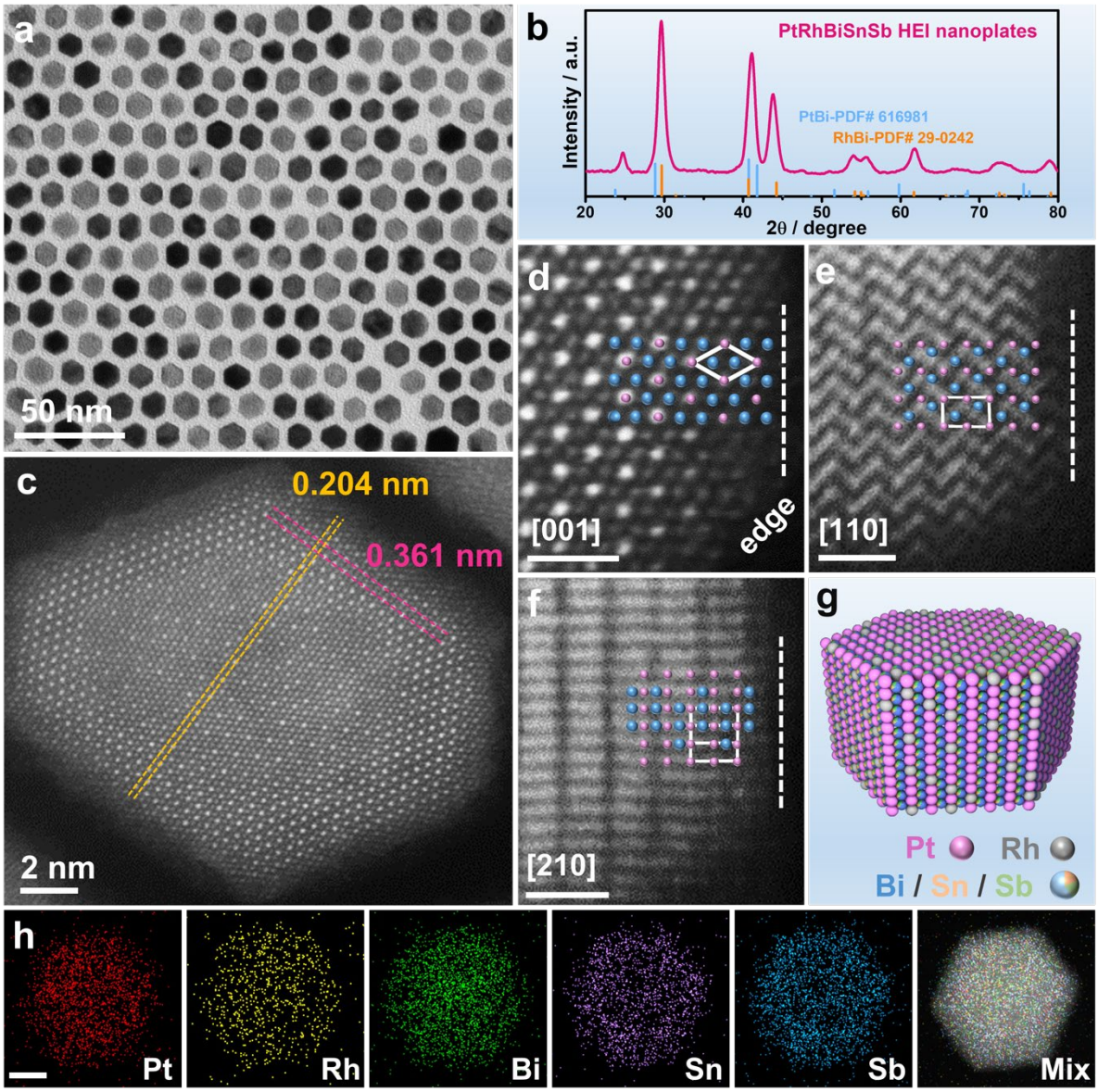

Figure 1. a) TEM image and b) XRD pattern of the PtRhBiSnSb HEI nanoplates. c-f) Typical aberration-corrected HAADF-STEM images of the surface of PtRhBiSnSb HEI nanoplates. The insets in (d-f) show the corresponding PtBi unit cells viewed along different zoom axes. The pink and blue spheres represent Pt and Bi atoms, respectively. Scale bars: 1 nm. g) The schematic illustration showing the atomic arrangement of Pt/Rh/Bi/Sn/Sb atoms on the surface of the PtRhBiSnSb HEI nanoplate. h) EDX mapping images of a PtRhBiSnSb HEI nanoplate. Scale bar: 5 nm.

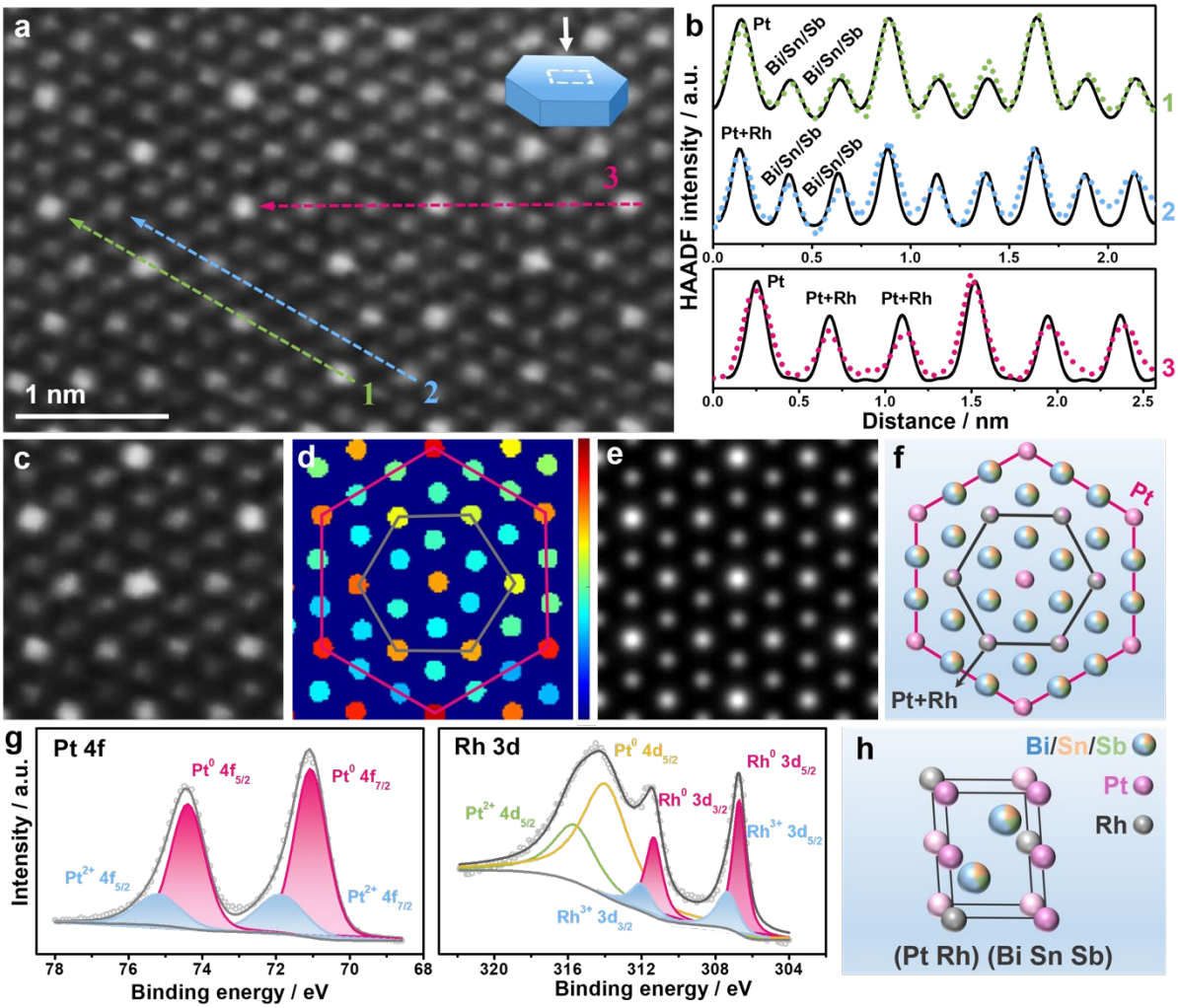

Figure 2. a) Typical aberration-corrected HAADF-STEM image of the center part of the PtRhBiSnSb HEI nanoplates. b) HAADF intensity line profiles (data points) taken along the appropriately numbered lines indicated in (a) (shown in scatter plots). Solid line plots are acquired from the corresponding image simulations (see Figure S11). c) HAADF image of the typical Rh-substituted Pt columns and (d) the corresponding color dots. e) Image simulation and (f) atomic model of the Rh-substituted Pt columns. g) Pt 4f and Rh 3d XPS spectra of the PtRhBiSnSb HEI nanoplates. h) Structural Model showing a crystallne unit of the (PtRh)(BiSnSb) HEI nanoplates.

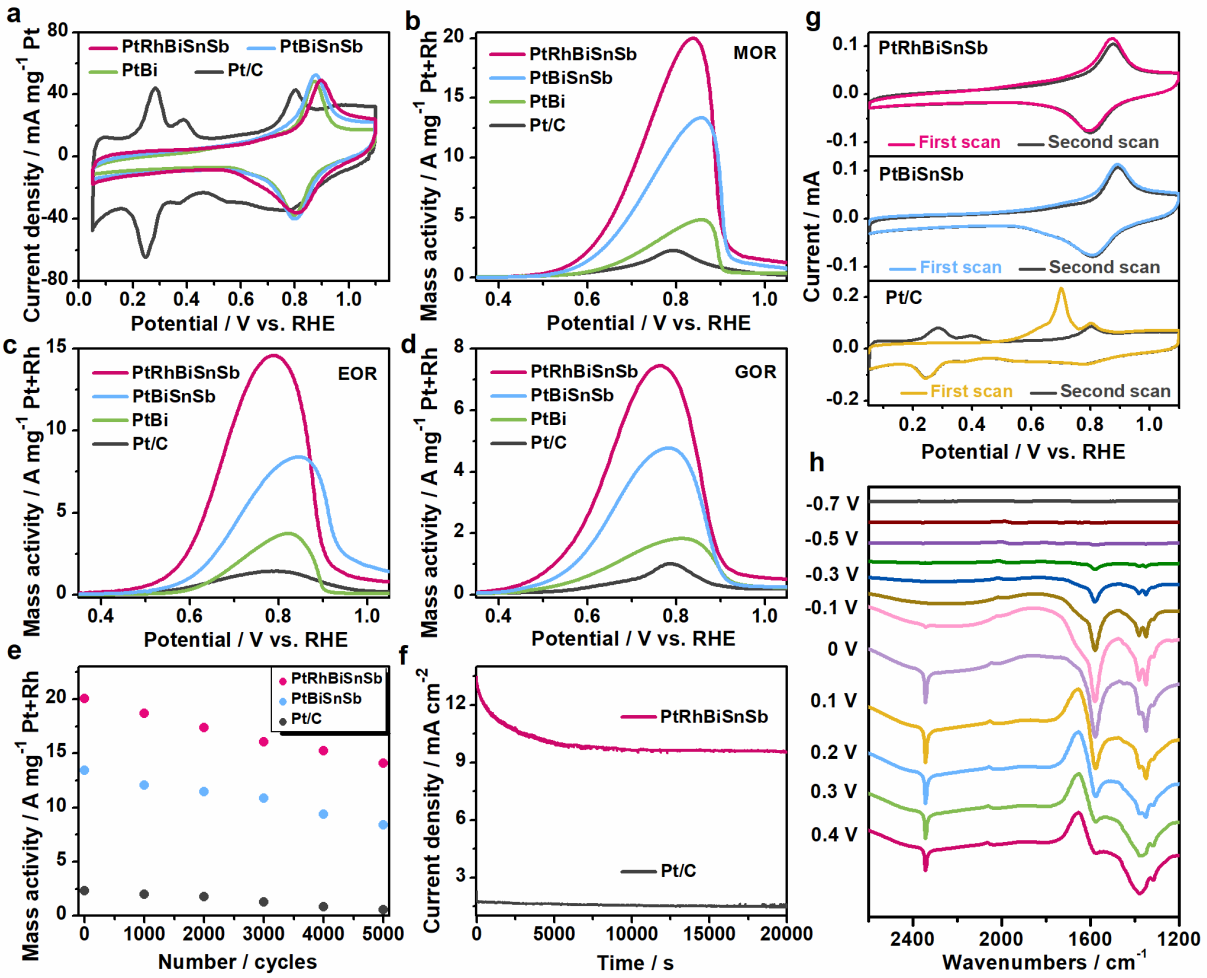

Figure 3. a) CV curves, (b) MOR, (c) EOR, and (d) GOR positive-going polarization curves of different catalysts recorded at a scan rate of 50 mV s^{-1}. e) The changes in mass activities of different catalysts before and after long-term potential cycling. f) Long-term chronoamperometry for MOR of different catalysts recorded at 0.7 V vs. RHE. g) CO-stripping curves of PtRhBiSnSb HEI nanoplates, PtBiSnSb nanoplates, and Pt/C catalysts recorded in Ar-saturated 1.0 M KOH at a scan rate of 50 mV s^{-1}. h) The in-situ FTIR spectra of PtRhBiSnSb HEI nanoplates recorded in Ar-saturated 1.0 M KOH + 1.0 M CH_3OH solution using a Hg/HgO as the reference electrode.

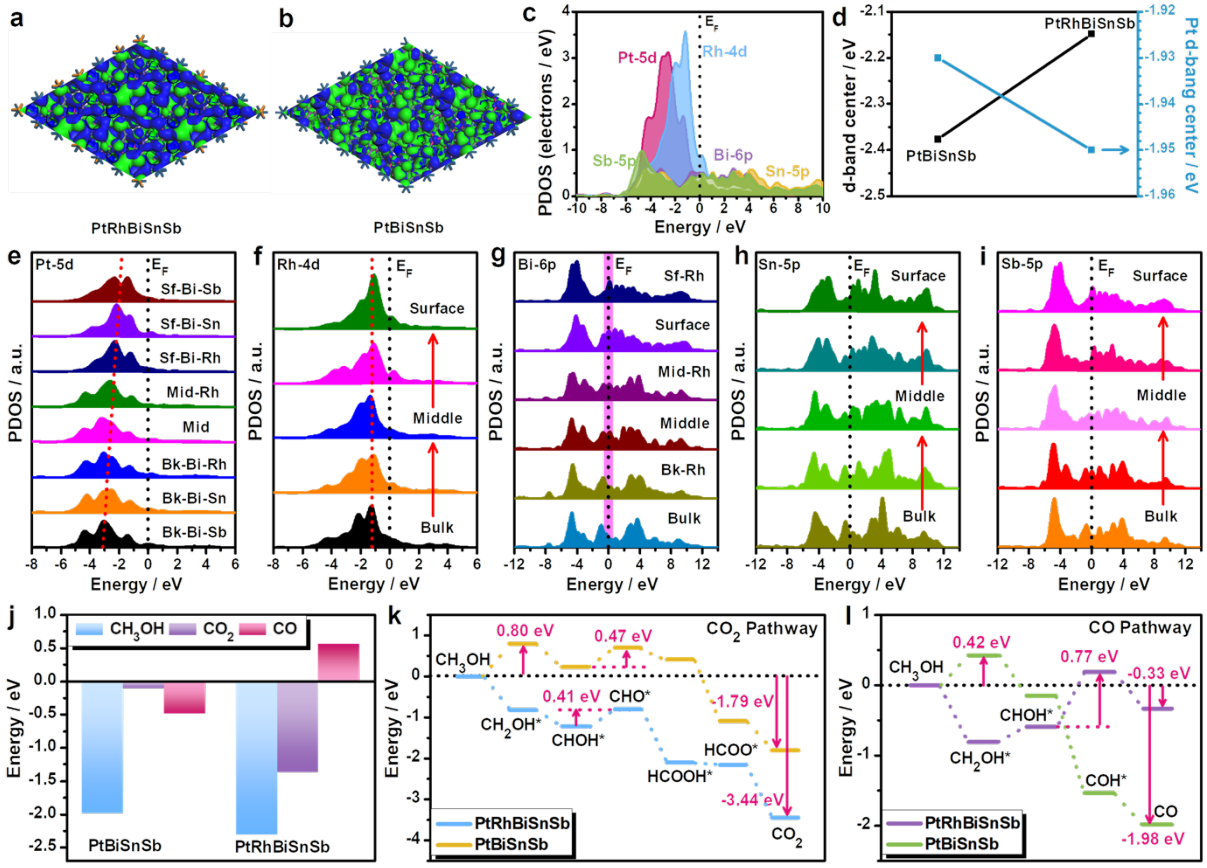

Figure 4. DFT calculations of the PtRhBiSnSb HEI nanoplates. 3D contour plot of electronic distributions near the Fermi level of (a) PtRhBiSnSb HEI nanoplates and (b) PtBiSnSb nanoplates from the top view. Blue, orange, purple, olive, and pink spheres represent Pt, Rh, Bi, Sn, and Sb atoms, respectively. c) PDOS of PtRhBiSnSb HEI nanoplates. d) The electronic structure comparison between PtRhBiSnSb HEI nanoplates and PtBiSnSb nanoplates. Site-dependent PDOSs of (e) Pt-5d, (f) Rh-4d, (g) Bi-6p, (h) Sn-5p, and (i) Sb-5p in PtRhBiSnSb HEI nanoplates. j) The adsorption energy comparison of CH_3OH, CO_2, and CO on PtRhBiSnSb HEI nanoplates and PtBiSnSb nanoplates. The reaction energy comparison of (k) CO_2 pathway and (l) CO pathway for MOR process on PtRhBiSnSb HEI nanoplates and PtBiSnSb nanoplates.

TOC

The high-entropy PtRhBiSnSb intermetallic nanoplates with intrinsically isolated Pt/Rh/Bi/Sn/Sb atoms are successfully constructed via a one-pot method. Benefiting from the synergism of chosen five elements, the well-defined PtRhBiSnSb intermetallic nanoplates achieve ultra-high performances towards the electrochemical oxidation of methanol, ethanol, and glycerol in alkaline electrolytes, emerging as a state-of-the-art multifunctional electrocatalyst for the alcohol oxidation reactions.

Keyword: high-entropy intermetallic; electrocatalysis; alcohol oxidation; nanocrystal.

Wen Chen#, Shuiping Luo#, Mingzi Sun#, Xiaoyu Wu, Yongsheng Zhou, Yujia Liao, Min Tang, Xiaokun Fan, Bolong Huang and Zewei Quan**

High-Entropy Intermetallic PtRhBiSnSb Nanoplates for Highly Efficient Alcohol Oxidation Electrocatalysis